Accurate Modeling of Coil Inductance for Near-Field Wireless Power Transfer

Accurate Modeling of Coil Inductance for Near Field Wireless Power Transfer

Sadeque Reza Khan, Sumanth Kumar Pavuluri and Marc P.Y. Desmulliez, *Senior Member, IEEE*

***Abstract*—This article presents closed form expressions for the self- and mutual inductances of circular wire wound coils used in near field wireless power transfer systems. The calculation of the radius of the coils, inspired from the Archimedean spiral found in many biological organisms, is used to model the self-inductance of single and multi-layer spiral coils. The value of the mutual inductance is determined by expressing the Taylor expansion of the Neumann's integral for constant current carrying wires. Formulas for mutual inductance are also derived for misaligned magnetically coupled coils enabling the rapid but accurate calculation of power transfer efficiency in real-life applications. Self- and mutual inductance values are computed using the 3D electromagnetic software package MAXWELL 3D™ and these values demonstrate excellent agreement compared with the proposed models. Wire wound coils of different geometrical configurations have been manufactured to validate experimentally the accuracy of the proposed models. Comparison of analytical and experimental results indicate that the proposed models are capable to accurately predict the self-inductance and mutual coupling rapidly. The proposed modeling paves the way for the time efficient optimization of near field wireless power transfer links.**

***Index Terms*—3D EM solver, multi-layer coil, misalignment, near field wireless power transfer, single-layer coil.**

I. Introduction

WIRELESS power transfer is utilized today in a wide range of applications, ranging from sophisticated low-power biomedical implants [1]–[4] to high-power electric vehicles [5]–[8]. The successful implementation of a wireless power link depends to some extent on the accurate modeling of the self- and mutual inductances that contribute to the optimization of the coupling coefficient between the primary transmission coil and the secondary receiver coil [9]. Achieving optimum power transfer efficiency and large tolerance to misalignment is today the subject of much research efforts [10]–[15].

This study was financially supported by the UK Engineering & Physical Research Council (EPSRC) under the programme grant *Sonopill* (EP/K034537/2) and Heriot-Watt University through the Doctoral Training Account (DTA) programme for International Students.

The authors are with the Institute of Sensors, Signals and Systems, School of Engineering and Physical Sciences, Heriot-Watt University, Edinburgh, EH14 4AS, Scotland, UK (e-mail: srk5@hw.ac.uk).

Several established methods for the calculation of the self-inductance exist in the literature [10],[16]–[25]. Most of these methods consider the current carrying loop as a set of concentric
circles. Consequently, there is always some discrepancy between the analytical expression of the self-inductance and the simulated and experimental results. Many contributions in literature have also been made to calculate the mutual inductance [26]–[29], predominantly in the case of perfectly aligned coils [30]–[32]. Analytical derivation of the mutual inductance for misaligned coils is however rare [24],[33],[34] and only carried out for translational misalignment despite the fact that angular misalignment in some applications can also drastically affect the mutual inductance and thus the power link performance. A complete analysis of the variation of the mutual inductance value that takes into account translational and angular misalignment is therefore needed for the accurate characterization of the performance of the wireless power transfer link.

3D electromagnetic (EM) field solution software is one of the most consistent approaches for computing self- and mutual inductance values [33]. However, the simulation of complex multi-loop and multi-planar wire wound coils (WWC) in a 3D EM solver requires substantial computational time. On the other hand, the previous semi-analytical approaches referenced above require long numerical operations which do not reduce the computational complexity [20],[26],[29],[30],[32]. In the light of these difficulties, this article presents a simple, yet accurate, method to estimate self- and mutual inductances to design and optimize a near field wireless power transfer link. In this study, the self-inductance is calculated using the Archimedean spiral geometry used for the coiling of WWCs. Furthermore, complex geometrical parameters are avoided and computationally efficient models are presented for the calculation of the mutual inductance. The proposed models have been verified by 3D EM simulation and validated experimentally. Various coil models have been designed and simulated in ANSYS MAXWELL 3D™. The software package is a commercial quasi-static solver [35], [36]. The magnetostatic simulation mode has been used to solve the coil models. The self-inductance of the same configurations has been measured using a Fluke PM6306 RCL meter and an auto-balancing bridge technique is adopted to measure the mutual inductance of the physical coils. The experimental

values obtained indicate excellent agreement with the proposed analytical models.

II. Self-Inductance

The self-inductance, L_{self}, of a single circular coil of loop radius, R, and wire diameter, w, can be represented as [10],[20]–[25]

$$L_{self}(R,w) = \mu R\left[ln\left(\frac{16R}{w}\right) - 2\right] \quad (1)$$

where μ is the permeability of the medium surrounding the coil. For two perfectly aligned coils of radii R_i and R_j, with center-to-centre distance, d_{ij}, the mutual inductance, M_{ij} can be calculated as [10], [20]

$$M_{ij} = M(R_i, R_j, d_{ij}) = \frac{2\mu}{\alpha_{ij}}\sqrt{R_i R_j}\left[\left(1 - \frac{\alpha_{ij}^2}{2}\right)K(\alpha_{ij}) - E(\alpha_{ij})\right] \quad (2)$$

with

$$\alpha_{ij} = 2\sqrt{\frac{R_i R_j}{(R_i + R_j)^2 + {d_{ij}}^2}} \quad (3)$$

where $K(\alpha_{ij})$ and $E(\alpha_{ij})$ are the complete elliptic integrals of the first and second kind, respectively.

A. Self-inductance of a single layer spiral coil (SLSC)

The continuously varying radius of the loop of a spiral coil needs to be calculated to determine the self-inductance of such a coil. The coil is in fact an Archimedean spiral [37]. As shown in Fig. 1, the calculated radius, R, is:

$$R = R_0 + \frac{w + s_l}{2\pi}\theta_R \quad (4)$$

where R_0 is the start radius, θ_R is the angle of revolution (=$2\pi j$ at the j^{th} loop forming thereby the radius R_j) and s_l is the space between two consecutive loops.

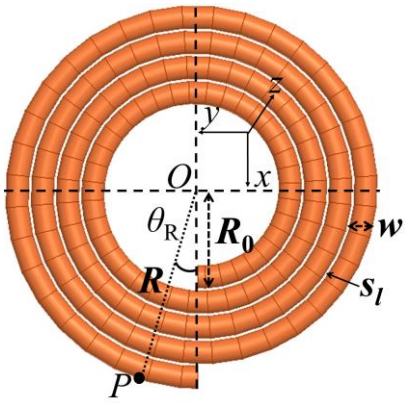

Fig. 1. Parameters to calculate the varying radius of a 4-loop single layer Archimedean spiral.

All the loops of a single-layer coil have a common center so that d_{ij}=0. The self-inductance of N_l loops, L_{self}, can be calculated from (1) and (2) as

$$L_{self} = \sum_{i=1}^{N_l} L(R_i, w) + \sum_{i=1}^{N_l}\sum_{j=1}^{N_l} M(R_i, R_j, 0) \times (1 - \delta_{ij}) \quad (5)$$

where δ_{ij}=1 *for* i=j; δ_{ij}=0, otherwise.

The behaviour of the self-inductance is compared in Fig. 2 for different outer diameters (or number of loops) of a coil, for wire diameter w=200 μm, starting radius R_0=2.19 mm and spacing s_l=10 μm, against results obtained with the 3D-EM field solution software package MAXWELL 3D™. The case of the ideal coil of same outer diameter but with concentric circles (labelled ideal CC) is also provided [10], [20]. The maximum percentage of variation with respect to the 3D EM simulation is also indicated on the same figure (right vertical axis). For the proposed model, the variation is less than 3% whereas the use of concentric circles produces a variation of around 45%. Therefore, the proposed model offers better accuracy in the approximation of L_{self}.

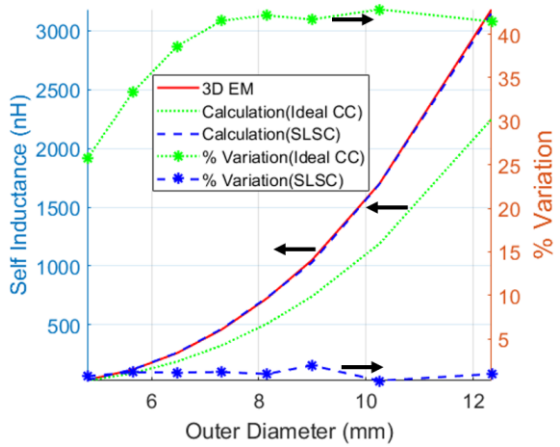

Fig. 2. L_{self} as a function of the outer diameter of the coil. The proposed new model is benchmarked against the 3D EM modeling software package and the idealized model where all circles are considered concentrical. The %variation with respect to the 3D EM values is also indicated for the ideal and proposed models.

B. Self-inductance of a Multi-Layer Helical Coil (MLHC)

Fig. 3 shows the model of a multi-loop, multi-layer helical coil where s_t represents the spacing between two consecutive layers in the vertical direction. L_i and T_j are the i^{th} loop and j^{th} layer, respectively.

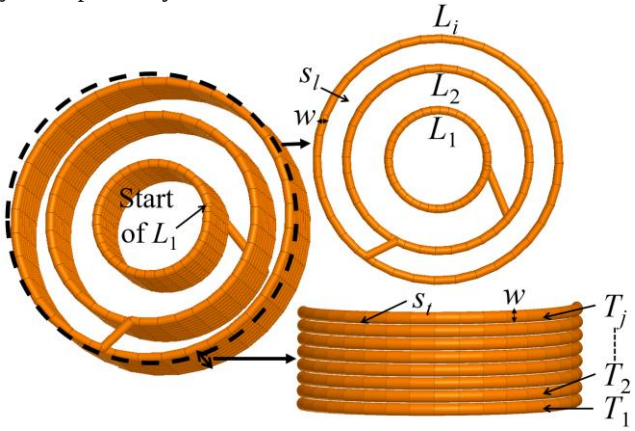

Fig. 3. Multi-loop and multi-layer helical coil. The spacing between two loops has been exaggerated to indicate the interconnection between the loops of the MLHC.

In this model, a loop L_1 of radius R_0 is formed initially with T_j layers going downwards. At the bottom of the coil, a second loop L_2 of radius R_1 is formed with T_j layers going upwards. At the top of the coil, the same process continues for loop L_i (= L_3) going downwards, etc. In this case, θ_R=2π(i–1) is used to estimate the radius of the L_i^{th} loop using equation (4). The distance between the reference layer T_1 and T_j, $d_{T_1T_j}$, is simply

$$d_{T_1T_j} = (j-1) \times (s_t + w) \tag{6}$$

For a coil with N_t layers and N_l loops per layer, the total self-inductance can be modeled as

$$L_{self} = N_t \sum_{i=1}^{N_l} L(R_i, w) + N_t \sum_{i=1}^{N_l} \sum_{j=1}^{N_l} M(R_i, R_j, 0) \times (1 - \delta_{ij}) + \sum_{i=1}^{(N_t-1)} \sum_{j=1}^{N_l} \sum_{k=1}^{N_l \times (N_t - i)} M\left(R_j, R_k, d_{T_iT_j}\right) \tag{7}$$

where δ_{ij} = 1 for $i = j$, δ_{ij} = 0, otherwise. The first term in (7) is the self-inductance of the N_t layers containing N_l loops each. The second term accounts for the mutual inductance effect of the loops for a single layer. The last term considers the mutual inductance of different loops of different layers with one layer always considered as a reference plane.

In Fig. 4, the performance of L_{self}, considered as an ideal CC and MLHC is benchmarked against the 3D EM simulation as a function of numbers of layers where N_l=2, w = 400 μm, D = 8.4 mm, s_t=10 μm and s_l=10 μm. This configuration is representative of biomedical implant applications such as capsule endoscopy [38]. The variation with respect to the EM software results, %variation, is around 12% for N_t=2, decreasing to less than 5% for a larger number of layers. Again, the proposed model shows better performance for a high number of N_l and N_t.

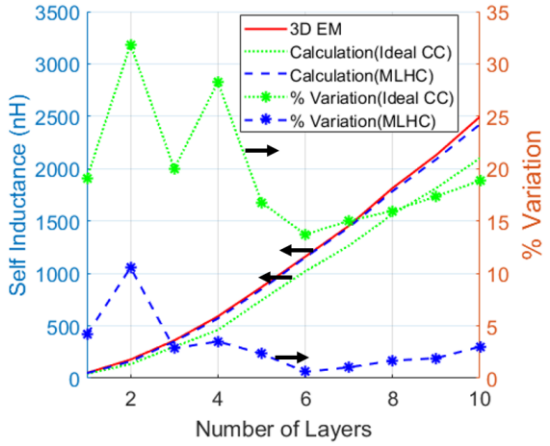

Fig. 4. L_{self} for different layers N_t of multi-layer helical coil using 3D EM simulation results, ideal (concentrical circles) model and proposed model.

$$M = \frac{\mu}{4\pi} \oint \oint \frac{\overrightarrow{dl_{C1}} \cdot \overrightarrow{dl_{C2}}}{R_p} \tag{8}$$

The magnitude, R_p, of the vector joining a point P on C1 to a point Q lying on C2, as shown in Fig. 5, is:

$$R_p = \left[\begin{matrix} R_{C1}^2 + R_{C2}^2 + d_r^2 \\ -2R_{C1}R_{C2}\cos(\varphi_{C1} - \varphi_{C2}) \end{matrix} \right]^{\frac{1}{2}} \tag{9}$$

where φ_{C1} and φ_{C2} are the angular co-ordinates of P on C1 and Q on C2, respectively. R_{C1} and R_{C2} are the radii of the coils C1 of wire diameter w_{C1}, and C2 of wire diameter w_{C2}, respectively. The relative center-to-center distance, d_r, between the coils where these points lie, can be approximated as

$$\begin{aligned} d_r = d_{r(N_{t,C1}, N_{t,C2})} = \\ d_1 + \left[(N_{t,C1} - 1) \times (w_{C1} + s_{t,C1})\right] \\ + \left[(N_{t,C2} - 1) \times (w_{C2} + s_{t,C2})\right] \end{aligned} \tag{10}$$

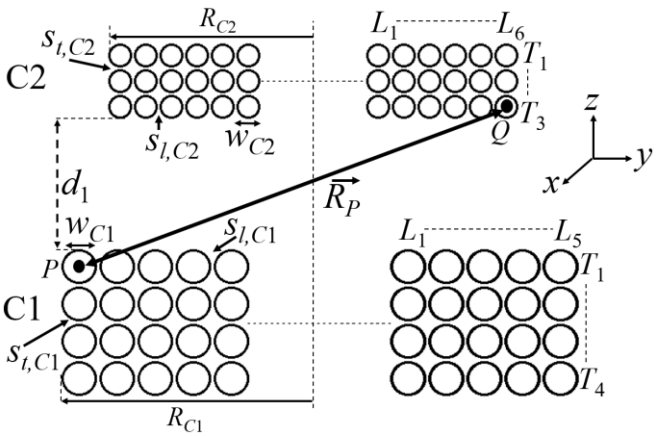

Fig. 5. Configuration of perfectly aligned coils. In this example, coil C1 has 5 loops and 4 layers. Coil C2 has 6 loops and 3 layers. Further, d_r=d_1 due to the choice of the points P and Q.

III. Mutual Inductance of Inductively Coupled Coils

In this section, the mutual inductance is modelled for perfectly aligned and misaligned inductively coupled coils. Results are compared with the 3D EM simulation.

A. *Case of perfectly aligned coils*

The mutual inductance, M, for two current carrying coils, C1 and C2, can be calculated using the Neumann's formula [26], [39]

where d_1 is the center-to-center distance for the top and bottom layers of C1 and C2, respectively. The point P lies on the $N_{t,C1}^{\text{th}}$ layer in C1 taking the reference layer as the top layer in Fig. 5. In the same way, the point Q lies in the $N_{t,C2}^{\text{th}}$ layer in C2 taking this time the bottom layer as the reference layer. Using (9) and the dot product of the two infinitesimal displacement vectors, dl_1 and dl_2, (8) can be rewritten as:

$$M = \frac{\mu}{4\pi} \frac{R_{C1}R_{C2}}{\sqrt{R_{C1}^2 + R_{C2}^2 + d_r^2}} \int_0^{2\pi} \int_0^{2\pi} \frac{\cos(\varphi_{C1} - \varphi_{C2})}{[1 - \gamma\cos(\varphi_{C1} - \varphi_{C2})]^{\frac{1}{2}}} d\varphi_{C1} d\varphi_{C2} \tag{11}$$

where γ [33] is

$$\gamma = \frac{2R_{C1}R_{C2}}{R_{C1}^2 + R_{C2}^2 + d_r^2} \tag{12}$$

Typical coils configurations used in WPT such as R_{C1}=30 mm and R_{C2}=4.2 mm and d_1=100 mm, provide a value of γ<<1.

The integrand inside (11) can therefore be linearized as a Taylor series up to the 5th order such that

$$M = \frac{\mu\pi R_{C1}^2 R_{C2}^2}{2(R_{C1}^2 + R_{C2}^2 + d_r^2)^{\frac{3}{2}}}\left[1 + \frac{15}{32}\gamma^2 + \frac{315}{1024}\gamma^4\right] \tag{13}$$

For a coil C1 containing T_{C1} layers and L_{C1} loops and a coil C2 containing T_{C2} layers and L_{C2} loops, the total mutual inductance is then

$$M_{total} = \sum_{i=1}^{T_{C1}}\sum_{j=1}^{T_{C2}}\sum_{k=1}^{L_{C1}}\sum_{l=1}^{L_{C2}} M(R_{C1:k}, R_{C2:l}, d_{r(i,j)}) \tag{14}$$

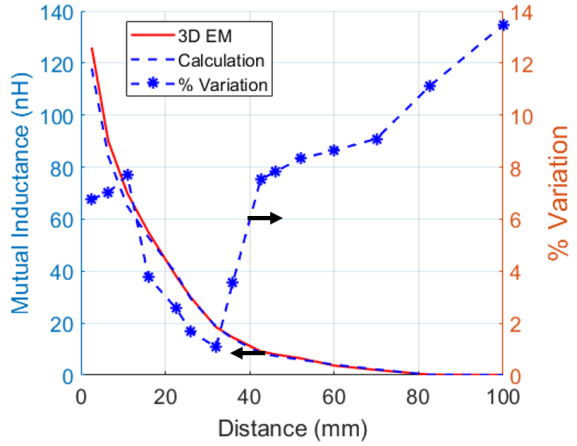

Fig. 6. M_{total} at different d_1 using 3D EM simulation results and proposed model. The percentage of variation with the software model is indicated on the right vertical axis.

where $R_{C1:k}$ and $R_{C2:l}$ are the radius of k^{th} loop of C1 and l^{th} loop of C2, respectively, and $d_{r(i,j)}$ is calculated according to (10).

Fig. 6 shows the value of the mutual inductance as a function of d_1 using the 3D EM simulation and (14). The coil radius for the two coils was calculated using (4). The total numbers of layers and loops were 12 and 1, respectively for C1, and 10 and 3, respectively for C2. The outer diameters for coils C1 and C2 were taken as 60 mm and 8.4 mm, respectively. The %variation between 3D EM simulation and proposed model is less than 10 % for separation distance less than 70 mm and increases to around 14% at d_1=100 mm.

B. *Case of translational misalignment*

Fig. 7 shows the configuration between C1 and C2 in the case of translational misalignment. C2 is off-axis by a distance, d_2, from the axis of the coil C1. The distance between two arbitrary points P and Q lying on C1 and C2, respectively, can be written as:

$$R_p = [R_{C1}^2 + R_{C2}^2 + d_r^2 + d_2^2 - 2R_{C1}R_{C2}\cos(\varphi_{C1} - \varphi_{C2}) - 2d_2R_{C1}\cos\varphi_{C1} + 2d_2R_{C2}\cos\varphi_{C2}]^{\frac{1}{2}} \tag{15}$$

To calculate the mutual inductance, the following parameters, γ_a, γ_b and γ_c are introduced:

$$\gamma_a = \frac{2R_{C1}R_{C2}}{R_{C1}^2 + R_{C2}^2 + d_r^2 + d_2^2} \tag{16}$$

$$\gamma_b = \frac{2R_{C1}d_2}{R_{C1}^2 + R_{C2}^2 + d_r^2 + d_2^2} \tag{17}$$

$$\gamma_c = \frac{2R_{C2}d_2}{R_{C1}^2 + R_{C2}^2 + d_r^2 + d_2^2} \tag{18}$$

Replacing (16), (17), (18) in (15) and using (8):

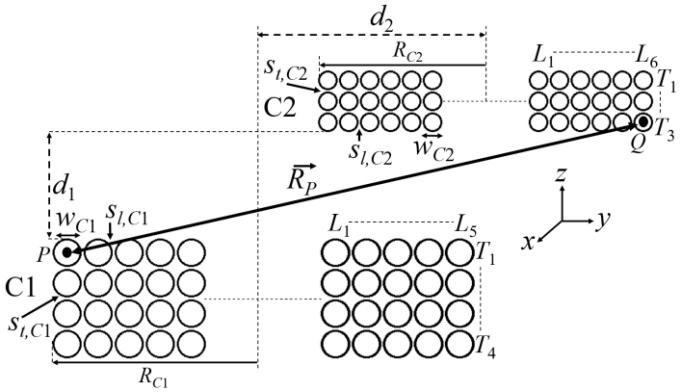

Fig. 7. Configuration of translational misalignment of C2. In this example, coil C1 has 5 loops and 4 layers. Coil C2 has 6 loops and 3 layers. Further, d_r=d_1 is considered.

$$M = \frac{\mu}{4\pi}\frac{R_{C1}R_{C2}}{\sqrt{R_{C1}^2 + R_{C2}^2 + d_r^2 + d_2^2}}\int_0^{2\pi}\int_0^{2\pi}\frac{\cos(\varphi_{C1} - \varphi_{C2})}{[1 - \gamma_a\cos(\varphi_{C1} - \varphi_{C2}) - \gamma_b\cos\varphi_{C1} + \gamma_c\cos\varphi_{C2}]^{\frac{1}{2}}}d\varphi_{C1}d\varphi_{C2} \tag{19}$$

The values of γ_a, γ_b and γ_c are less than unity for traditional WWC configurations. Linearizing again the denominator of (19) using a Taylor series expansion to the 4th order and integrating

$$M = \frac{\mu\pi R_{C1}^2 R_{C2}^2}{2(R_{C1}^2 + R_{C2}^2 + d_r^2 + d_2^2)^{\frac{3}{2}}}\left[1 - \frac{3}{2}\delta + \frac{15}{32}\gamma_a^2\left(1 - \frac{21}{2}\delta\right) + \frac{15}{16}(\gamma_b^2 + \gamma_c^2)\left(1 - \frac{7}{4}\delta\right)\right] \quad (20)$$

where

$$\delta = \frac{d_2^2}{R_{C1}^2 + R_{C2}^2 + d_r^2 + d_2^2} \quad (21)$$

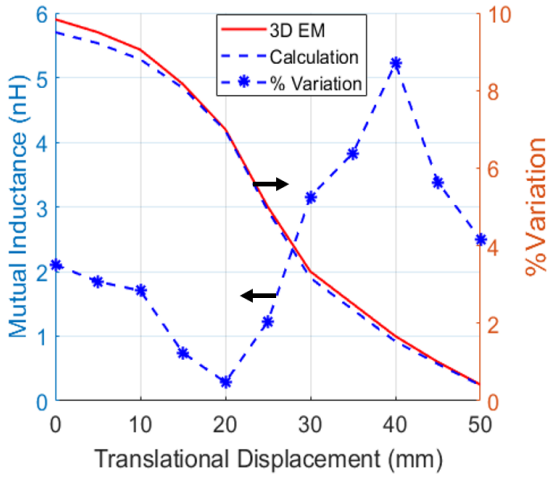

Fig. 8. M_{total} at different translational displacements d_2, for d_1=50 mm using 3D EM simulation results and proposed model. The percentage of variation of the values of the proposed model with respect to the simulation results is indicated on the right vertical axis.

Note that, when d_2=0, which is the case of perfectly aligned coils, the expression of M from (13) is recovered up to the third order. The total mutual inductance, M_{total}, can be calculated as

$$M_{total} = \sum_{i=1}^{T_{C1}}\sum_{j=1}^{T_{C2}}\sum_{k=1}^{L_{C1}}\sum_{l=1}^{L_{C2}} M\begin{pmatrix} R_{C1:k}, R_{C2:l}, \\ d_{r(i,j)}, d_2 \end{pmatrix} \quad (22)$$

Fig. 8 shows the variation of M_{total} between C1 and C2 at d_1=50 mm for d_2 ranging from 0 to 50 mm using the 3D EM simulation software and (22). The coil parameters are the same as in the case of perfectly aligned coils. The %variation between 3D EM simulation and proposed model is less than 9%.

C. *Case of angular misalignment*

The configuration of coils suffering from angular misalignment is shown in Fig. 9. Angular misalignment can be due to roll and pitch rotations which are represented in the figure by θ and λ, respectively. The distance between two arbitrary point lying on C1 and C2 can be written as

$$R_p = \left[\begin{matrix} R_{C1}^2 + R_{C2}^2 + d_r^2 - 2R_{C1}R_{C2}(\cos\varphi_{C1}\cos\varphi_{C2}\cos\theta\cos\lambda + \sin\varphi_{C1}\sin\varphi_{C2}) - 2d_r R_{C2}\cos\varphi_{C2} \\ (\sin\theta\cos\lambda + \sin\lambda\cos\theta) + 2R_{C2}^2\cos^2\varphi_{C2}\sin\theta\cos\lambda\sin\lambda\cos\theta \end{matrix}\right]^{\frac{1}{2}} \quad (23)$$

The parameters γ_a, γ_b and γ_c are introduced as

$$\gamma_a = \frac{2R_{C1}R_{C2}}{R_{C1}^2 + R_{C2}^2 + d_r^2} \quad (24)$$

$$\gamma_b = \frac{2R_{C2}d_r}{R_{C1}^2 + R_{C2}^2 + d_r^2} \quad (25)$$

$$\gamma_c = \frac{2R_{C2}^2}{R_{C1}^2 + R_{C2}^2 + d_r^2} \quad (26)$$

The values of γ_a, γ_b and γ_c are less than unity for wireless power application. Replacing (24), (25) and (26) in (23) the modified M from (8) can be written as

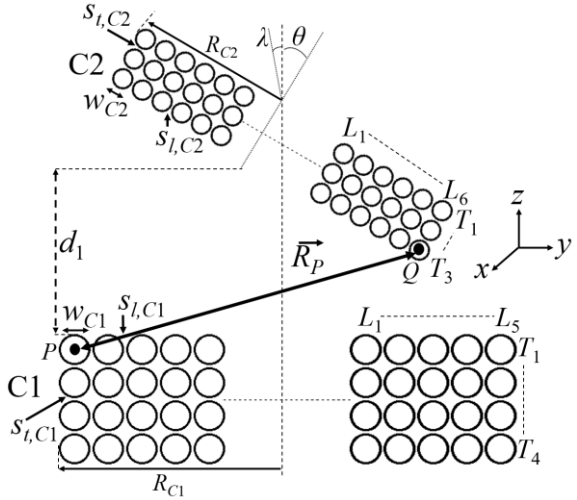

Fig. 9. Configuration of angular misalignment. In this example, coil C1 has 5 loops and 4 layers. Coil C2 has 6 loops and 3 layers. Further, d_r=d_1 is considered.

$$M = \frac{\mu}{4\pi}\frac{R_{C1}R_{C2}}{\sqrt{R_{C1}^2 + R_{C2}^2 + d_r^2}}\int_0^{2\pi}\int_0^{2\pi}\frac{(\sin\varphi_{C1}\sin\varphi_{C2}\cos\theta\cos\lambda + \cos\varphi_{C1}\cos\varphi_{C2})}{\left[\begin{matrix}1 - \gamma_a(\cos\varphi_{C1}\cos\varphi_{C2}\cos\theta\cos\lambda + \sin\varphi_{C1}\sin\varphi_{C2} - \gamma_b\cos\varphi_{C2}) \\ (\sin\theta\cos\lambda + \sin\lambda\cos\theta) + \gamma_c\cos^2\varphi_{C2}\sin\theta\cos\lambda\sin\lambda\cos\theta\end{matrix}\right]^{\frac{1}{2}}} d\varphi_{C1}d\varphi_{C2} \quad (27)$$

The Taylor expansion of M can be written as:

$$M = \frac{\mu\pi R_{C1}^2 R_{C2}^2 \cos\theta\cos\lambda}{2(R_{C1}^2 + R_{C2}^2 + d_r^2)^{\frac{3}{2}}}\left[1 + \frac{15}{64}\gamma_a^2 + \frac{15}{64}\gamma_a^2\cos^2\theta\cos^2\lambda + \frac{15}{8}\gamma_b^2(\sin\theta\cos\lambda\sin\lambda\cos\theta)\right] \quad (28)$$

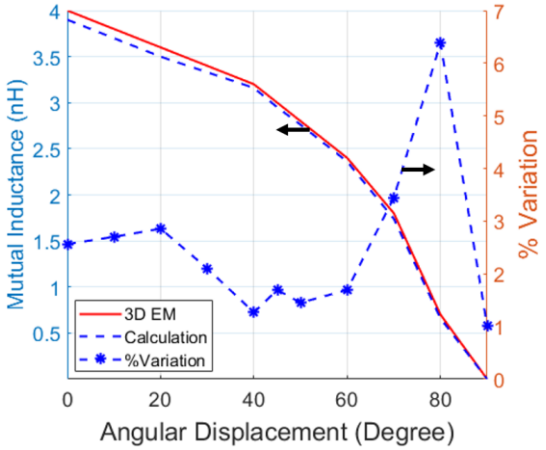

Fig. 10. M_{total} at different θ for λ=45° and d_1=50 mm using 3D EM simulation results and the proposed model. The percentage of variation of the values of the proposed model with respect to the simulation results is indicated on the right vertical axis.

Note that, when θ=λ=0, which is the case of perfectly aligned coils, the expression of M from (13) is recovered up to the third order. M_{total} can be written as

$$M_{total} = \sum_{i=1}^{T_{C1}}\sum_{j=1}^{T_{C2}}\sum_{k=1}^{L_{C1}}\sum_{l=1}^{L_{C2}} M\begin{pmatrix} R_{C1:k}, R_{C2:l}, \\ d_{r(i,j)}, \theta, \lambda \end{pmatrix} \quad (29)$$

Fig. 10 shows the changes of M_{total} for d_1=50 mm as a function of θ (with λ fixed at 45°) using 3D EM simulation and (29) using the same coil parameters as in the previous section. Allowing independent variations of θ and λ, the maximum % variation with respect to the simulation model is also less than 7%. The changes of M_{total} as a function of θ and d_1 (for λ=45°) using (29) are provided in Fig.11. A 3D plot using the 3D EM simulation provides similar results. The minimum and maximum differences between the two surfaces occur at θ=60° and d_1=40 mm (4% variation) and θ=80° and d_1=100 mm (13% variation), respectively.

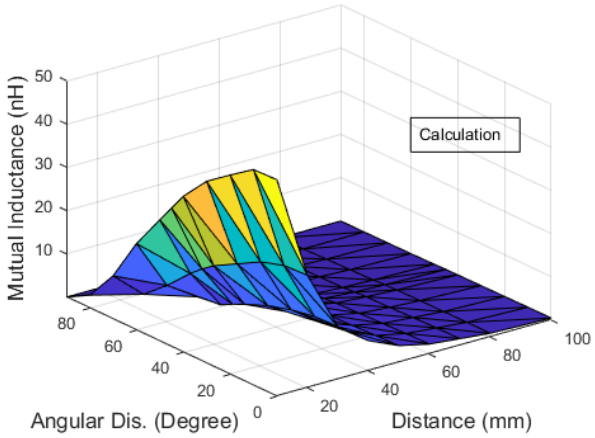

Fig. 11. M_{total} at different θ and d_1 for λ=45° using the analytical model.

D. *Case of translational and angular misalignment*

The configuration in the case of combined translational and angular misalignment is shown in Fig. 12. The distance between two arbitrary points of C1 and C2 is approximated such that:

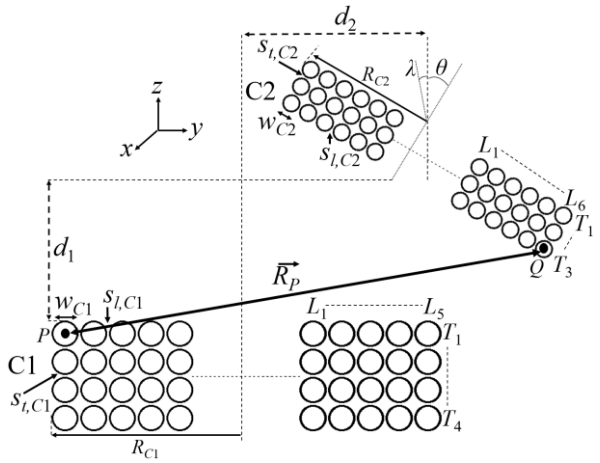

Fig. 12. Configuration of the coil for translational and angular misalignment. In this example, coil C1 has 5 loops and 4 layers. Coil C2 has 6 loops and 3 layers. Further, d_r=d_1 is taken in to the consideration.

$$R_p = \begin{bmatrix} R_{C1}^2 + R_{C2}^2 + d_r^2 + d_2^2 - 2R_{C1}R_{C2}(\cos\varphi_{C1}\cos\varphi_{C2}\cos\theta\cos\lambda + \sin\varphi_{C1}\sin\varphi_{C2}) \\ -2d_rR_{C2}\cos\varphi_{C2}(\sin\theta\cos\lambda + \sin\lambda\cos\theta) - 2d_2R_{C1}\cos\varphi_{C1} + 2d_2R_{C2}\cos\varphi_{C2}\cos\theta \\ \cos\lambda + 2R_{C2}^2\cos^2\varphi_{C2}\sin\theta\cos\lambda\sin\lambda\cos\theta \end{bmatrix}^{\frac{1}{2}} \quad (30)$$

For simplification, the parameters γ_a, γ_b, γ_c, γ_d and γ_e are introduced as

$$\gamma_a = \frac{2R_{C1}R_{C2}}{R_{C1}^2 + R_{C2}^2 + d_r^2 + d_2^2} \quad (31)$$

$$\gamma_b = \frac{2R_{C1}d_2}{R_{C1}^2 + R_{C2}^2 + d_r^2 + d_2^2} \quad (32)$$

$$\gamma_c = \frac{2R_{C2}d_2}{R_{C1}^2 + R_{C2}^2 + d_r^2 + d_2^2} \quad (33)$$

$$\gamma_d = \frac{2R_{C2}d_r}{R_{C1}^2 + R_{C2}^2 + d_r^2 + d_2^2} \quad (34)$$

$$\gamma_e = \frac{2R_{C2}^2}{R_{C1}^2 + R_{C2}^2 + d_r^2 + d_2^2} \quad (35)$$

These parameters are smaller than unity for the wireless power transfer coils. Replacing (31), (32), (33), (34) and (35) in (30) the modified M from (8) can be written as

$$M=\frac{\mu}{4\pi}\frac{R_{C1}R_{C2}}{\sqrt{R_{C1}^2+R_{C2}^2+d_r^2+d_2^2}}\int_0^{2\pi}\int_0^{2\pi}\frac{(\sin\varphi_{C1}\sin\varphi_{C2}\cos\theta\cos\lambda+\cos\varphi_{C1}\cos\varphi_{C2})}{\left[\begin{matrix}1-\gamma_a(\cos\varphi_{C1}\cos\varphi_{C2}\cos\theta\cos\lambda+\sin\varphi_{C1}\sin\varphi_{C2})-\gamma_b\cos\varphi_{C1}\\+\gamma_c\cos\varphi_{C2}\cos\theta\cos\lambda-\gamma_d\cos\varphi_{C2}(\sin\theta\cos\lambda+\sin\lambda\cos\theta)\\+\gamma_e\cos^2\varphi_{C2}\sin\theta\cos\lambda\sin\lambda\cos\theta\end{matrix}\right]^{\frac{1}{2}}}d\varphi_{C1}d\varphi_{C2} \quad (36)$$

Finally, the Taylor expansion of M is

$$M=\frac{\mu\pi R_{C1}^2R_{C2}^2\cos\theta\cos\lambda}{2(R_{C1}^2+R_{C2}^2+d_r^2+d_2^2)^{\frac{3}{2}}}\left[\begin{matrix}1+\frac{15}{64}(\gamma_a^2+4\gamma_b^2)+\frac{15}{64}(\gamma_a^2+4\gamma_c^2)\cos^2\theta\cos^2\lambda+\frac{15}{8}\gamma_d^2(\sin\theta\cos\lambda\sin\lambda\cos\theta)\\-\frac{15}{8}\gamma_c\gamma_d\cos\theta\cos\lambda(\sin\theta\cos\lambda+\sin\lambda\cos\theta)-\frac{3}{2}(\delta_a-\delta_b(\tan\theta+\tan\lambda))\end{matrix}\right] \quad (37)$$

where

$$\delta_a=\frac{d_2^2}{R_{C1}^2+R_{C2}^2+d_r^2+d_2^2} \quad (38)$$

$$\delta_b=\frac{d_2d_r}{R_{C1}^2+R_{C2}^2+d_r^2+d_2^2} \quad (39)$$

Furthermore, M_{total} can be expressed as:

$$M_{total}=\sum_{i=1}^{T_{C1}}\sum_{j=1}^{T_{C2}}\sum_{k=1}^{L_{C1}}\sum_{l=1}^{L_{C2}}M\left(\begin{matrix}R_{C1:k},R_{C2:l},\\d_{r(i,j)},d_2,\theta,\lambda\end{matrix}\right) \quad (40)$$

M_{total} between C1 and C2 was calculated at d_1=50 mm for d_2 varying from 0 to 50 mm, and θ from 0 to 90° (with λ=45°) using (40) and 3D EM simulation. Paramters for the coils are the same as in the previous section. The %variation between 3D EM simulation and proposed model is less than 10% over the complete range of d_2 and angles.

IV. Experimental Setup

As listed in Table I, various coils have been hand-made to validate the proposed models using copper wire of different wire diameters, number of layers and numbers of loops. A Fluke PM6306 RCL meter was used to measure L_{self} of the assembled coils.

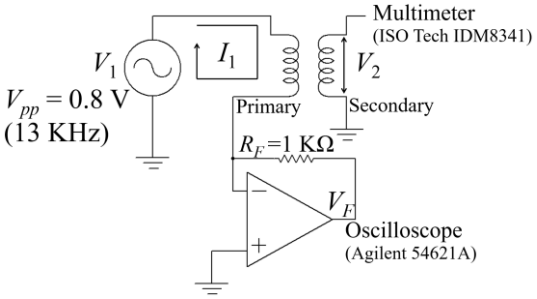

Fig. 13. Schematic view of the experimental setup for the measurement of the mutual inductance.

TABLE I
Coil Properties

Coil Type	R (mm)	w (μm)	N_l	N_t
Single loop single layer	30	1000	5	1
Single loop multi-layer	5.2	560	1	12
Multi-loop multi-layer	7.5	720	3	5

Fig. 13 shows the schematic of the experimental setup for the measurement of the mutual inductance. Two sets of coils, SLSC and MLHC, reported in Table I, are used as secondary coils to experimentally validate the mutual inductance model. The primary coil is a single layer coil made of 6 loops with R=43.75 mm and w=1 mm. An auto-balancing bridge is used to measure the mutual inductance. The voltage drop across the primary coil is V_1 and output voltage of the amplifier is V_F. The operational amplifier is connected in a differentiator configuration and used as a negative impedance converter. The amplifier sinks the input current of inverting port through R_F resistor connected in the output. I_1 is the current through the primary coil and induces a voltage V_2 in the secondary side. The transfer impedance seen at the secondary coil is

$$|Z|=\left|\frac{V_2}{I_1}\right|=\left|\frac{-V_2R_F}{V_F}\right| \quad (41)$$

Therefore,

$$M=\frac{|Z|}{2\pi f} \quad (42)$$

where f is the frequency of the input signal.

V. Experimental Results

Fig. 14 shows the measured values of L_{self} for the SLSC presented in Table I with varying outer diameters.

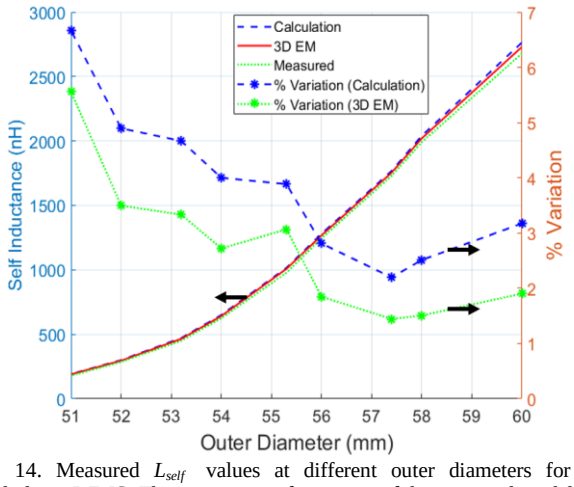

Fig. 14. Measured L_{self} values at different outer diameters for the single-layer WWC. The percentage of variation of the proposed model and 3D EM simulation with respect to the measured results is indicated on the

right vertical axis.

The measured result is compared with the simulation and the proposed model. The %variation of the model and the 3D EM simulation with respect to measured results is presented on the right vertical axis and show the %variation is less than 7% for both the proposed model and 3D EM simulation

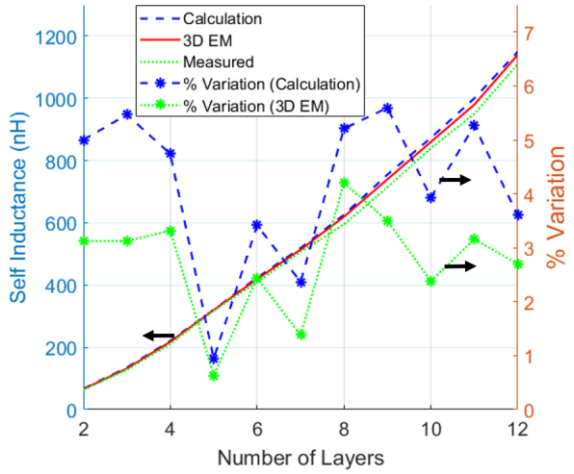

Fig. 15. Measured L_{self} values for multi-layer, single loop coils and comparison with the proposed model and 3D EM simulation results. The percentage of variation of the values of the proposed model and 3D EM simulation with respect to the measured results is indicated on the right vertical axis.

Fig. 15 shows the measured values of L_{self} for the multi-layer single loop case presented in Table I as the number of layers vary. The %variation of the experimental results with respect to both the proposed and 3D EM simulation models is less than 6%.

Fig. 16 presents the experimental and simulation results of L_{self} for the multi-loop, multi-layer (N_t=5) coil as the number of loops is varied from 1 to 5. The variation for both the proposed and 3D EM simulation models with respect to experimental values is less than 8%.

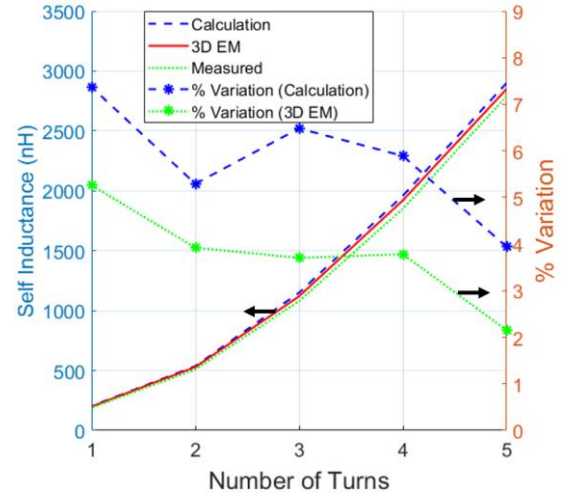

Fig. 16. Measured L_{self} values as a function of the number of loops for the multi-loop (N_t=5) WWC and comparison with the proposed model and 3D EM simulation results. The percentage of variation for the proposed model and 3D EM simulation with respect to the measured results is indicated on the right vertical axis.

Fig. 17 shows the measurement results in comparison with (14) and 3D EM simulation for perfectly aligned single layer primary and secondary coils. The %variation occurring with respect to the proposed model is less than 3.5% for single layer coils. Similar plot of multi-layer coils demonstrates less than 10% variation for the proposed model.

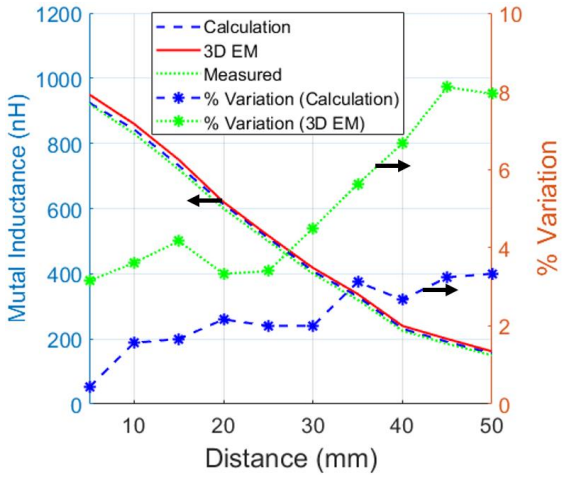

Fig. 17. Measurement of M_{total} at different d_1 and comparison with proposed model and 3D EM simulation results for perfectly aligned single layer primary and secondary coils. The %variation of the proposed model and 3D EM simulation with respect to measured results are presented in the right vertical axis.

Fig. 18 shows the magnetic field distribution of perfectly aligned single layer primary and secondary coils. In Fig. 18 (a), d_1=10 mm, the secondary coil is strongly exposed to the magnetic field radiation of the primary coil due to smaller center-to-center distance. Figs. 18 (b) and (c) demonstrate lower magnetic field intensity in the secondary coil due to the larger separation distance (d_1=35 and 50 mm, respectively) of the primary coil. This confirms the reduction of M_{total} due to the increase in d_1.

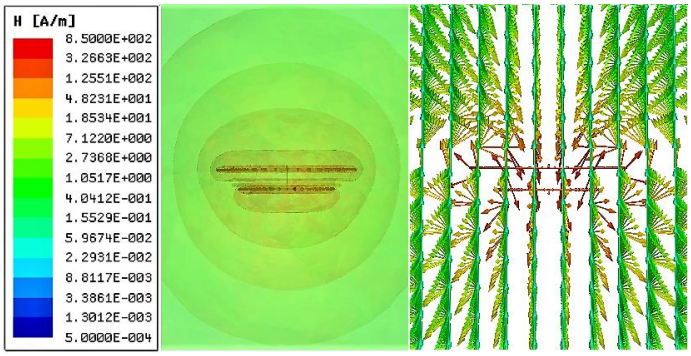

(a)

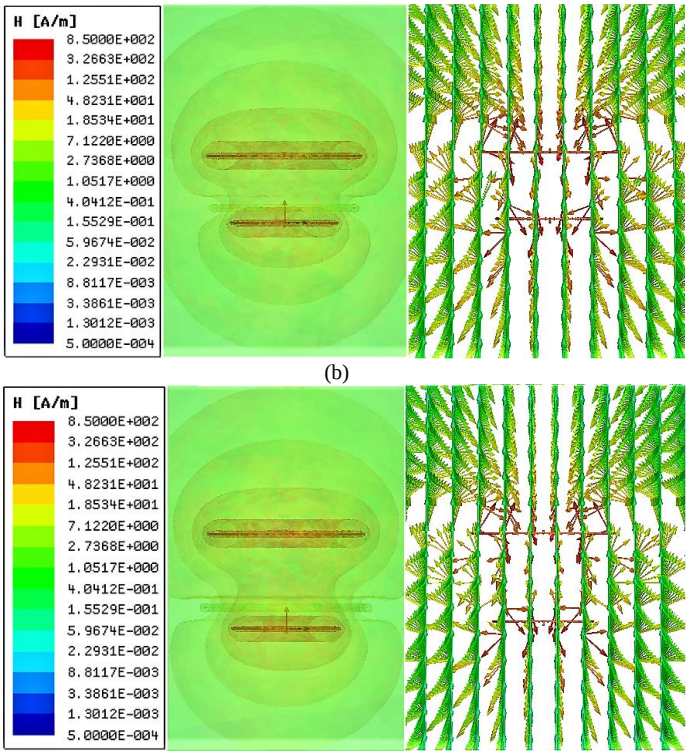

Fig. 18. Magnetic field distribution for perfectly aligned coils. (a) d_1=10 mm. (b) d_1=35 mm. (c) d_1=50 mm.

Fig. 19 presents the measured and 3D EM simulated results for different translational misalignment distances, d_2, for d_1=10mm for single layer primary and secondary coils. The variation in the proposed model remains less than 3%. The same type of measurement for multi-layer coils can show a %variation of slightly over 6%.

Figs. 20 (a) and (b) show the magnetic field distribution for d_2=10 and 30 mm, respectively, for d_1=10 mm. The field intensity in the secondary coil due to primary coil is lower in both cases compared to Fig. 18 (a), causing thereby a reduction of the M_{total}.

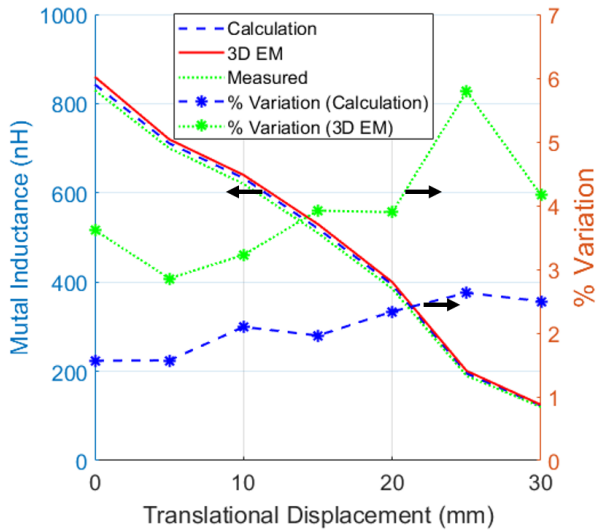

Fig. 19. Measurement of M_{total} values at different translational displacement d_2 for d_1 = 10 mm and comparison with the proposed model and 3D EM simulation results for single layer primary and secondary coils. The %variation of the proposed model and 3D EM simulation with respect to measured results are presented in the right vertical axis.

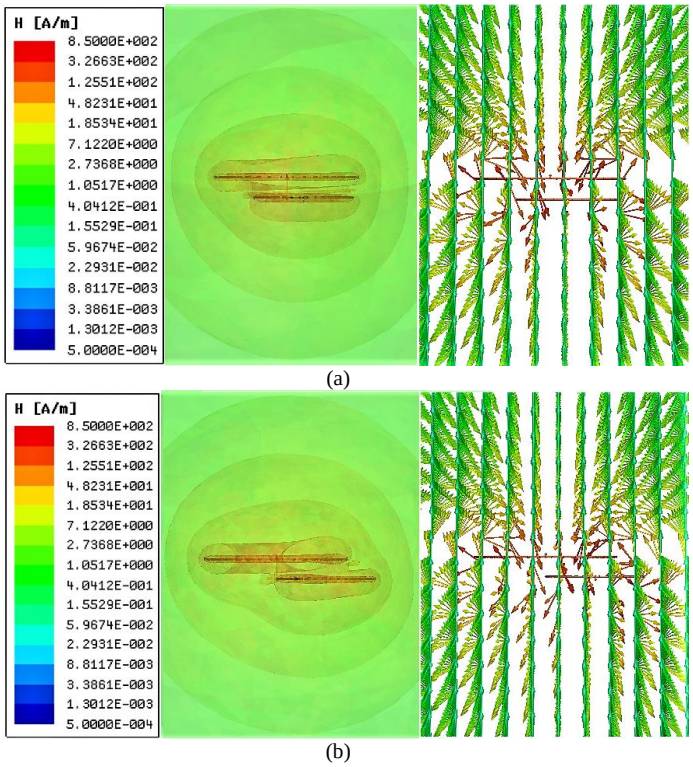

Fig. 20. Magnetic field distribution for translational misalignment for d_1 = 10 mm. (a) d_2=10 mm. (b) d_2=30 mm.

Fig. 21 shows the measured, calculated (29) and 3D EM simulated results of angular misalignment for single-layer primary and secondary coils. The roll rotation angle, θ is changed for a constant pitch rotation angle λ=30°. The %variation remains less than 6.5% for the proposed model and 3D EM simulation for single layer coils. In the case of multi-layer coils, the percentage variation is around 8%.

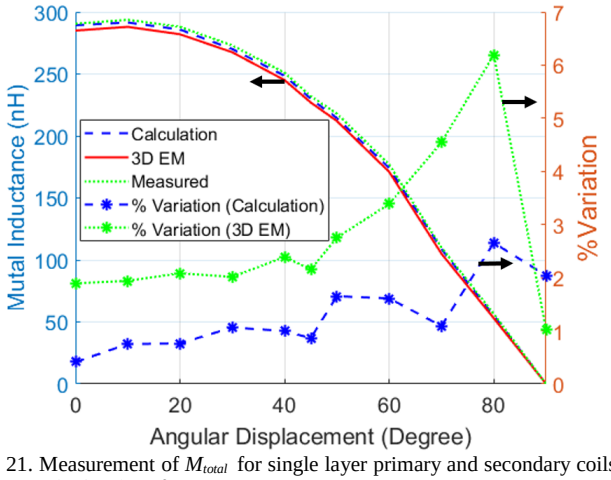

Fig. 21. Measurement of M_{total} for single layer primary and secondary coils at different θ for λ=30° and d_1=35 mm. The proposed model and 3D EM simulation results are also compared. The %variation of the proposed model with respect to measured results are presented in the right vertical axis.

Further, Fig. 22 shows the measured, calculated (29) and 3D EM simulated results of varying θ with respect to constant λ=45° and d_1=35 mm. The observed %variation is less than 7% for the proposed model and 3D EM simulation for single layer coils. In the case of similar plot of multi-layer coil, this percentage variation is raised up to 10%.

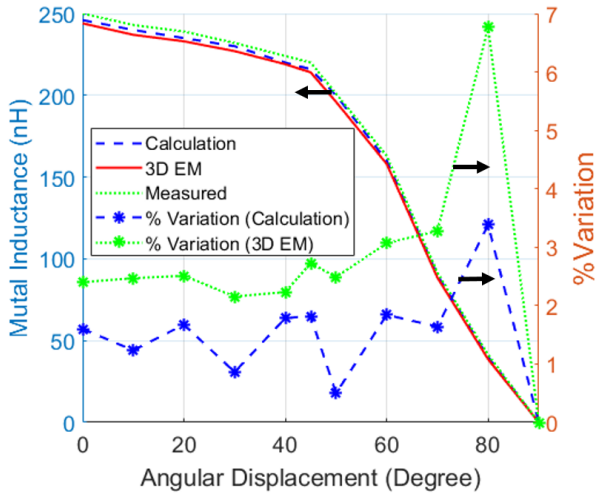

Fig. 22. Measurement of M_{total} for single layer primary and secondary coils at different θ for λ=45° and d_1=35 mm. The proposed model and 3D EM simulation results are also compared. The %variation of the proposed model with respect to measured results are presented in the right vertical axis.

In Fig. 23, the measured, calculated (29) and 3D EM simulated results are illustrated for varying θ with respect to constant λ=60° and d_1=35 mm. The %variation is close to 5% for the proposed model and 3D EM simulation for single layer coils. This percentage variation is less than 11% for the similar plot of multi-layer coil.

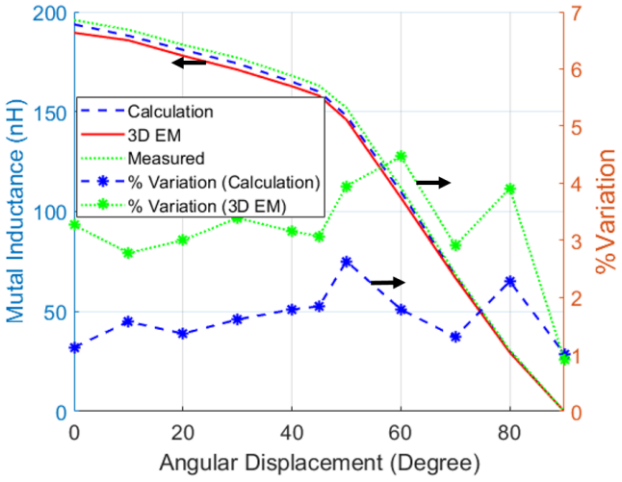

Fig. 23. Measurement of M_{total} for single layer primary and secondary coils at different θ for λ=60° and d_1=35 mm. The proposed model and 3D EM simulation results are also compared. The %variation of the proposed model with respect to measured results are presented in the right vertical axis.

Figs. 24 (a), (b), (c) and (d) show the magnetic field distribution for θ=λ=30°, θ=λ=45°, θ=λ=60° and θ=λ=90°, respectively, for d_1=35 mm. Compared to Fig. 18 (b) the exposure of the magnetic radiation from primary coil reduces with the gradually increasing θ and λ of the secondary coil.

TABLE II
COMPARISON OF THE SIMULATION TIMES

Configuration of the coil(s)	Simulation Time (3D EM)	Simulation Time (Proposed Model)
L_{self}, single layer	10 min	12×10^{-3} s
L_{self}, single loop multi-layer	15 min	15×10^{-3} s
L_{self}, multi-loop multi-layer	45 min	18×10^{-3} s
M_{total}, perfectly aligned (single layer secondary coil)	6 hr 30 min	2.3 s
M_{total}, translational misaligned (single layer secondary coil)	5 hr 45 min	2.1 s
M, angularly misaligned (single layer secondary coil)	5hr 30 min	2.4 s
M, incorporated misaligned (single layer secondary coil)	12 hr 40 min	5 s

M_{total} reduces therefore significantly. In case of θ=λ=90°, the field vectors of primary coil are in parallel with the position of the secondary coil bringing M_{total} close to zero.

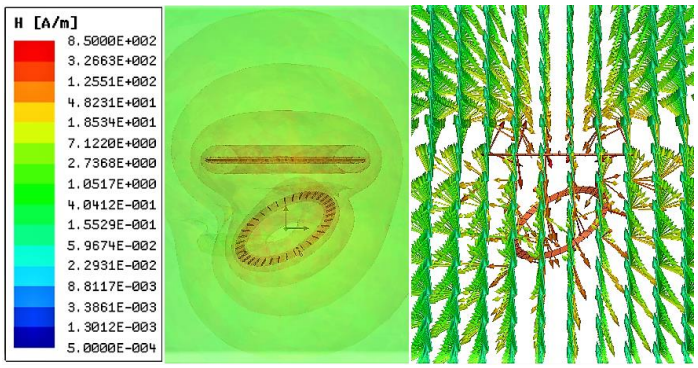

(a)

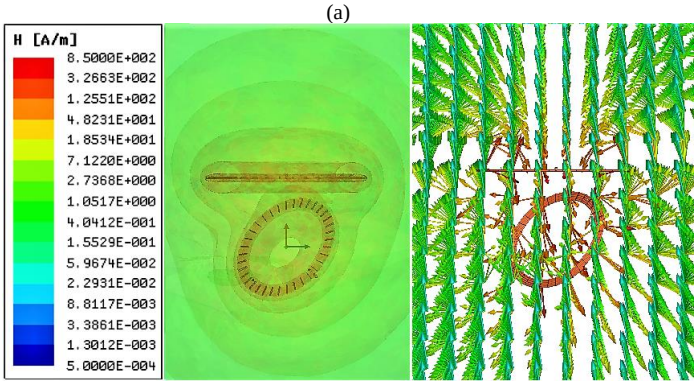

(b)

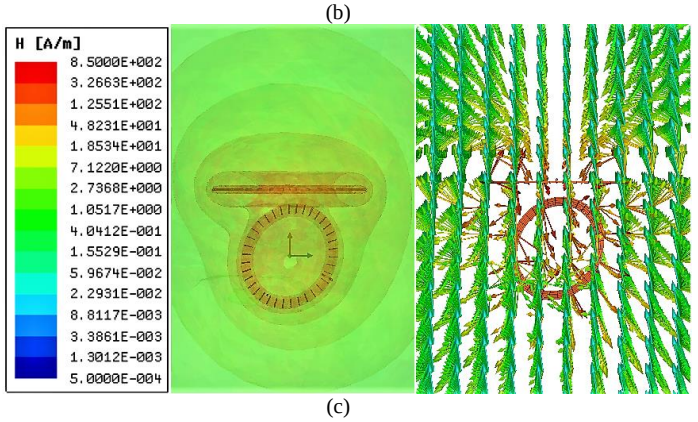

(c)

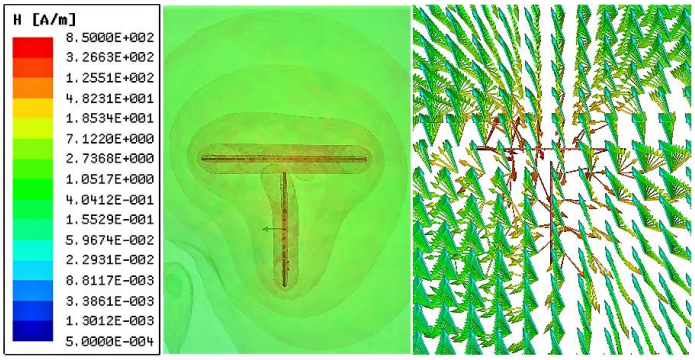

(d)

Fig. 24. Magnetic field distribution for angular misalignment at d_1 = 35 mm. (a) θ=λ=30°. (b) θ=λ=45°.(c) θ=λ=60°. (d) θ=λ=90°.

The calculation of M_{total} at different d_2 and θ ranging from 0 to 90° (λ=45°, d_1=35 mm) for the single layer secondary coil has also been conducted. The %variation of the measured results with the proposed model (40) and 3D EM simulation are less than 3% and 5.5%, respectively.

The proposed model is designed for near field wireless power transfer applications. It is observed that the simulated M depends on the frequency. This is mainly caused by the parasitic effects near the self-resonant frequency of the coil [33]. In Table I, the single layer coil has a self-resonance frequency over 40 MHz. A variation of less than 10% between the analytical and simulated M is recorded in the complete kHz frequency range. This variation increases up to 15% at 20 MHz, 20% near 30 MHz and 34.5% at 40 MHz. The multi-layer coil shows a variation over 25% near their self-resonant frequency (over 30 MHz). It is therefore recommended that the analytical model be used only up to half the self-resonant frequency of the coil studied.

VI. Computational Efficiency

Table II provides a comparison of the computational time required for the proposed analytical model (MATLAB™) and the 3D EM software (MAXWELL 3D™) using parameters for the coils manufactured for this study. The simulation was performed on an Intel (R) Xeon (R) CPU E5-2640 with processor speed of 2.5 GHz and 128 GB of RAM (HP Z820 workstation). The comparison confirms that a significant amount of simulation time can be saved using the models proposed in this paper.

VII. Conclusions

This paper presents an accurate modeling method of the self-inductance, and compact solutions for the calculation of the mutual inductance for near field wireless power transfer systems. The detailed mathematical derivation of inductances is presented. The proposed models have been compared with the 3D EM simulation results for numerical validation and experimentally validated. This method shows excellent prediction capability of self-inductance for all types of WWC coils (single and multi-layer). Additionally, it provides a cost-effective calculation for the determination of the mutual inductance values at any separation distance and misalignment cases. Self- and mutual inductance of different assembled coils are measured and compared with the proposed prediction models. Results demonstrate an excellent agreement in the accuracy of the proposed models. The comparison of the required computational time also proves the efficiency of the proposed models. Therefore, the self- and mutual inductance models presented in this paper can be considered as an excellent candidate for the design and optimization of sophisticated near field wireless power transfer systems.

References

[1] Guoxing Wang, Wentai Liu, M. Sivaprakasam, and G. A. Kendir, "Design and analysis of an adaptive transcutaneous power telemetry for biomedical implants," *IEEE Trans. Circuits Syst. I Regul. Pap.*, vol. 52, no. 10, pp. 2109–2117, Oct. 2005.

[2] C. Sauer, M. Stanacevic, G. Cauwenberghs, and N. Thakor, "Power harvesting and telemetry in CMOS for implanted devices," *IEEE Trans. Circuits Syst. I Regul. Pap.*, vol. 52, no. 12, pp. 2605–2613, Dec. 2005.

[3] F. Inanlou and M. Ghovanloo, "Wideband Near-Field Data Transmission Using Pulse Harmonic Modulation," *IEEE Trans. Circuits Syst. I Regul. Pap.*, vol. 58, no. 1, pp. 186–195, Jan. 2011.

[4] M. Ghovanloo and K. Najafi, "A Modular 32-site wireless neural stimulation microsystem," *IEEE J. Solid-State Circuits*, vol. 39, no. 12, pp. 2457–2466, Dec. 2004.

[5] J. Sallan, J. L. Villa, A. Llombart, and J. F. Sanz, "Optimal Design of ICPT Systems Applied to Electric Vehicle Battery Charge," *IEEE Trans. Ind. Electron.*, vol. 56, no. 6, pp. 2140–2149, Jun. 2009.

[6] J. L. Villa, J. Sallán, A. Llombart, and J. F. Sanz, "Design of a high frequency Inductively Coupled Power Transfer system for electric vehicle battery charge," *Appl. Energy*, vol. 86, no. 3, pp. 355–363, 2009.

[7] C.-S. Wang, G. A. Covic, and O. H. Stielau, "Power Transfer Capability and Bifurcation Phenomena of Loosely Coupled Inductive Power Transfer Systems," *IEEE Trans. Ind. Electron.*, vol. 51, no. 1, pp. 148–157, Feb. 2004.

[8] C.-S. Wang, O. H. Stielau, and G. A. Covic, "Design Considerations for a Contactless Electric Vehicle Battery Charger," *IEEE Trans. Ind. Electron.*, vol. 52, no. 5, pp. 1308–1314, Oct. 2005.

[9] S. I. Babic and C. Akyel, "Calculating Mutual Inductance Between Circular Coils With Inclined Axes in Air," *IEEE Trans. Magn.*, vol. 44, no. 7, pp. 1743–1750, Jul. 2008.

[10] A. K. RamRakhyani, S. Mirabbasi, M. Chiao, and C. M, "Design and optimization of resonance-based efficient wireless power delivery systems for biomedical implants.," *IEEE Trans. Biomed. Circuits Syst.*, vol. 5, no. 1, pp. 48–63, 2011.

[11] S. R. Khan and G. S. Choi, "Analysis and optimization of four-coil planar magnetically coupled printed spiral resonators," *Sensors (Switzerland)*, vol. 16, no. 8, 2016.

[12] U.-M. Jow and M. Ghovanloo, "Design and Optimization of Printed Spiral Coils for Efficient Transcutaneous Inductive Power Transmission," *IEEE Trans. Biomed. Circuits Syst.*, vol. 1, no. 3, pp. 193–202, Sep. 2007.

[13] G. Pan, W. Xin, G. Yan, and J. Chen, "A video wireless capsule endoscopy system powered wirelessly: design, analysis and experiment," *Meas. Sci. Technol.*, vol. 22, no. 6, p. 65802, 2011.

[14] G. Pan and L. Wang, "Swallowable wireless capsule endoscopy: Progress and technical challenges," *Gastroenterol. Res. Pract.*, vol. 2012, 2012.

[15] K. Na, H. Jang, H. Ma, and F. Bien, "Tracking optimal efficiency of magnetic resonance wireless power transfer system for biomedical capsule endoscopy," *IEEE Trans. Microw. Theory Tech.*, vol. 63, no. 1, pp. 295–303, 2015.

[16] N. Sadiku, *Elements of Electromagnetics*. Orlando, FL: Sounders College Press, 1994.

[17] Z. Yang, W. Liu, and E. Basham, "Inductor modeling in wireless links for implantable electronics," *IEEE Trans. Magn.*, vol. 43, no. 10, pp. 3851–3860, 2007.

[18] M. Kiani, U. M. Jow, and M. Ghovanloo, "Design and Optimization of a 3 Coil Inductive Link for Efficient Wireless Power Transmission," *IEEE Trans. Biomed. Circuits Syst.*, vol. 5, no. 6, pp.

579–591, 2011.
[19] M. Kiani and M. Ghovanloo, "A figure-of-merit for designing high-performance inductive power transmission links," *IEEE Trans. Ind. Electron.*, vol. 60, no. 11, pp. 5292–5305, 2013.
[20] C. M. Zierhofer and E. S. Hochmair, "Geometric approach for coupling enhancement of magnetically coupled coils," *IEEE Trans. Biomed. Eng.*, vol. 43, no. 7, pp. 708–714, 1996.
[21] S. Atluri and M. Ghovanloo, "Design of a wideband power-efficient inductive wireless link for implantable biomedical devices using multiple carriers BT - 2nd International IEEE EMBS Conference on Neural Engineering, 2005, March 16, 2005 - March 19, 2005," vol. 2005, pp. 533–537, 2005.
[22] X. Li *et al.*, "A wireless magnetic resonance energy transfer system for micro implantable medical sensors," *Sensors (Switzerland)*, vol. 12, no. 8, pp. 10292–10308, 2012.
[23] Y. Yi, U. Buttner, Y. Fan, and I. G. Foulds, "Design and optimization of 3-coil resonance-based wireless power transfer system for biomedical implants," *Int. J. Circuit Theory Appl.*, vol. 43, pp. 1379–1390, 2015.
[24] T. P. Duong and J. W. Lee, "A dynamically adaptable impedance-matching system for midrange wireless power transfer with misalignment," *Energies*, vol. 8, no. 8, pp. 7593–7617, 2015.
[25] D. H. Kim, J. Kim, and Y. J. Park, "Optimization and Design of Small Circular Coils in a Magnetically Coupled Wireless Power Transfer System in the Megahertz Frequency," *IEEE Trans. Microw. Theory Tech.*, vol. 64, no. 8, pp. 2652–2663, 2016.
[26] F. W. Grover, *Inductance calculations : working formulas and tables*. Dover Publications, 1946.
[27] C. Snow, "Formulas for Computing Capacitance and Inductance," *National Bureau of Standards Circular*, vol. 544. p. 1, 1954.
[28] H. B. Dwight, *Electrical coils and conductors*. New York: McGraw-Hill, 1945.
[29] M. Soma, D. Galbraith, and R. L. White, "Radio-frequency coils in implantable devices: misalignment analysis and design procedure," *IEEE Trans. Biomed. Eng.*, vol. BME-34, no. 4, pp. 276–282.
[30] K. B. Kim, E. Levi, Z. Zabar, and L. Birenbaum, "Mutual inductance of noncoaxial circular coils with constant current density," *IEEE Trans. Magn.*, vol. 33, no. 5 PART 3, pp. 4303–4309, 1997.
[31] S. I. Babic and C. Akyel, "New analytic-numerical solutions for the mutual inductance of two coaxial circular coils with rectangular cross section in air," *IEEE Trans. Magn.*, vol. 42, no. 6, pp. 1661–1669, 2006.
[32] W. G. Hurley, M. C. Duffy, J. Zhang, I. Lope, B. Kunz, and W. H. Wolfle, "A Unified Approach to the Calculation of Self- and Mutual-Inductance for Coaxial Coils in Air," *IEEE Trans. Power Electron.*, vol. 30, no. 11, pp. 6155–6162, 2015.
[33] S. Raju, S. Member, R. Wu, M. Chan, C. P. Yue, and S. Member, "Modeling of Mutual Coupling Between Planar Inductors in Wireless Power Applications," vol. 29, no. 1, pp. 481–490, 2014.
[34] S. Reza Khan and G. Choi, "Optimization of planar strongly coupled wireless power transfer system for biomedical applications," *Microw. Opt. Technol. Lett.*, vol. 58, no. 8, pp. 1861–1866, Aug. 2016.
[35] S. N. Makarov, G. M. Noetscher, and A. Nazarian, *Low-frequency electromagnetic modeling for electrical and biological systems using MATLAB*. John Wiley & Sons, Inc, 2015.
[36] S. Makarov, G. Noetscher, T. Raij, and A. Nummenmaa, "A Quasi-Static Boundary Element Approach with Fast Multipole Acceleration for High-Resolution Bioelectromagnetic Models," *IEEE Trans. Biomed. Eng.*, pp. 1–1, 2018.
[37] S. Coombes, "The Geometry and Pigmentation of Seashells," *Techn. Ber. Dep. Math. Sci. Univ. Nottingham*, pp. 1–4, 2009.
[38] J. Faerber *et al.*, "In Vivo Characterization of a Wireless Telemetry Module for a Capsule Endoscopy System Utilizing a Conformal Antenna," *IEEE Trans. Biomed. Circuits Syst.*, pp. 1–11, 2017.
[39] D. J. Griffiths, *Introduction To Electrodynamics*, 3rd ed. Prentice-Hall, 1999.

Sadeque Reza Khan received his BSc degree in electronics and telecommunication engineering from University of Liberal Arts Bangladesh on 2010 and M.Tech degree in VLSI design from National Institute of Technology Karnataka, India in 2014. He is currently pursuing Ph.D. degree in electrical engineering at Heriot-Watt University, UK.

Sumanth Kumar Pavuluri received a Ph.D. degree from Heriot-Watt University, Edinburgh, UK, in 2011. He is currently a post-doctoral research associate at Heriot-Watt University working on microwave sensing, micro machined antennas, microwave applicators for curing and heating applications.

Marc Desmulliez (SM'87) received a Ph.D. in optoelectronics form Heriot-Watt University in 1995. He is currently Professor of Microsystems Engineering at Heriot-Watt University and leads the Multi-modal Sensing and Micro-Manipulation Research Group.